

# Subsampled scanning holographic imaging (SuSHI) for fast, non-adaptive recording of three-dimensional objects

ANTONY C. S. CHAN, KEVIN K. TSIA, AND EDMUND Y. LAM\*

Department of Electrical and Electronic Engineering, The University of Hong Kong, Pokfulam, Hong Kong, China

\*Corresponding author: elam@eee.hku.hk

Received 1 June 2016; revised 22 July 2016; accepted 22 July 2016 (Doc. ID 267547); published 10 August 2016

Optical scanning holography enables the recording of three-dimensional (3D) objects involving scattering or fluorescence emission. However, the time-consuming raster scanning process prevents real-time tracking of dynamic events. We propose a compressed sensing approach to reduce the number of measurements required by scanning only along a low-density spiral trajectory, thus reducing the acquisition time. Through simulation-based performance characterization, we show that the 3D objects can be accurately restored with only 4% of holographic measurements. We also apply spiral scanning to actual holographic systems to show five to twenty-five times speed improvement in the imaging frame rate with high reconstruction fidelity. This approach thus would be critically important for single-pixel holographic recording of dynamic events, including microbead tracking and optical sectioning of 3D scenes. © 2016 Optical Society of America

**OCIS codes:** (110.1758) Computational imaging; (090.1995) Digital holography; (100.3020) Image reconstruction-restoration.

<http://dx.doi.org/10.1364/OPTICA.3.000911>

## 1. INTRODUCTION

Digital holographic imaging is a powerful technology that captures a three-dimensional (3D) scene by recording the diffracted wavefront in a two-dimensional (2D) plane with an electronic sensor. To preserve both the amplitude and phase of the complex wavefront, a reference optical beam is often required in the Mach–Zehnder interferometer setup to interfere with the diffracted wavefront [1]. However, this configuration requires the diffracted light to have a high optical intensity and a long coherent length, comparable to that of the reference light in the setup. These requirements have limited its applications in imaging modalities involving weak scattering or fluorescence emission, where speckle noise is dominant [2]. To combat both intensity and coherence issues, common-path incoherent interferometry was proposed, where the reference beam is generated *in situ* either from the directly transmitted light through the 3D scene [3–5] or by wavefront shaping of the diffracted light [6,7]. Despite its promising performance, these configurations require a relatively strong diffraction effect from the specimen. Hence, it is restricted to microscopic applications, where the object size must be comparable to the illumination wavelength.

An alternative configuration, proposed by Poon and Korpel, places the Mach–Zehnder setup before the 3D object. This technique, known as optical scanning holography (OSH) [8,9], generates a time-varying Fresnel zone plate (FZP) that illuminates and scans the object, while the recorded scene is captured by a wide-area single-pixel camera (Fig. 1). Compared to the

common-path technique, this unique approach further bypasses the requirement of the diffraction effect in holographic image formation. It has since sparked interest ranging from speckle-free remote sensing on the millimeter scale [10] to fluorescence holographic microscopy on the micrometer scale [11,12].

Unlike other camera-based holographic setups, OSH requires 2D raster scanning to capture a single hologram. Hence, it is traditionally limited to capturing stationary 3D objects [8,10,12]. The design problem of high-speed raster scanning has two aspects: limited mechanical inertia of the scanning hardware, and the limited photon budget of photo detection. The former affects macroscopic imaging with wide-angle scanning systems, whereas the latter is more pronounced in microscopy systems where the received light intensity is low. In this paper, we propose a compressed sensing (CS) approach to reduce the acquisition time by scanning the object with a low-density non-raster trajectory. The smooth trajectory enables the maximum driving speed of the scanning hardware, which accounts for the acquisition speed up. In the case of a weak optical signal, where the long pixel dwell time dominates the scanning cycles, the shorter scanning trajectory still improves the time resolution of the dynamic events. The low-density trajectory also minimizes the laser exposure time. This is an important requirement in biological fluorescence imaging, as it alleviates the risk of photodamage and fluorescence bleaching of the biological specimen.

This CS implementation distinguishes itself from camera-based compressive holography, which compacts 3D objects either

to a single hologram [13] or to a fraction of pixels randomly selected in the hologram plane [14–17]. In 2D scanning systems, the subsampled pixels must form a continuous path in order for time reduction to be effective. In fact, the non-raster (e.g., spiral) trajectory design is inspired by compressed sensing magnetic resonance imaging, where the 3D volume capture is also restricted to a continuous scanning trajectory [18]. However, it is worth noting that a low-density trajectory also alleviates the throughput of holographic data due to the reduced overlapping of FZP illumination over the course of scanning [19]. Although data reduction is not the main scope of this paper, the observed data reduction ratio is comparable to the adaptive byte-stream compression method on the digitizer side [20,21].

We wish to emphasize that our method is not restricted to Fresnel holographic imaging only. The low-density spiral scanning approach is, in principle, generic to various illumination patterns. For instance, the depth-invariant FZP pattern, which is realized by an additional quadratic phase mask in the Mach–Zehnder interferometer, can be simply scanned with the low-density spiral trajectory to speed up extended depth-of-field imaging [22]. There are ongoing developments in advanced illumination patterns for specialized applications, ranging from improved lateral resolution [23] and depth resolution [24,25] to image encryption [26,27] and edge enhancement [28,29]. Therefore, we name our technique “subsampling scanning holographic imaging (SuSHI)” to reflect its wider applicability. This technique would be critically important for single-pixel holographic recording of dynamic events such as large-volume 3D fluorescence-stained cell migration [30] and non-Brownian microbeads motion tracking [31].

## 2. WORKING PRINCIPLE

### A. Holographic Imaging Process

The imaging process is depicted in Fig. 1. The time-varying FZP illumination pattern is projected onto the 3D scene by the 2D galvo-scanning system. The scattered light from the scene is

collected by the focusing lens before being captured by the wide-area single-pixel detector. The modulation frequency of the FZP is set to be much higher than the lateral scan rate, which results in optical beating of the collected scattered light. The amplitude and phase of the integrated signal thus can be extracted by the digital lock-in amplification process. The principle is the same for fluorescence holographic imaging applications, in which a long-pass optical filter is placed before the focusing lens to filter out the excitation wavelength before collection and phase retrieval. The hardware implementations of the time-varying FZP generation and lock-in phase extraction are discussed in Supplement 1.

While the single-pixel acquisition process integrates the optical intensity of the 3D scene, the galvo-mirror pair laterally shifts the FZP to different spatial locations during the recording. In other words, the measured signal is a 2D convolution of the FZP and multiple cross-sections of the 3D scene, which can be expressed as

$$I(x, y) = \sum_i [b(x, y, z_i) * O(x, y, z_i)] + n(x, y), \quad (1)$$

where  $I(x, y)$  is the measured complex-valued hologram,  $O(x, y, z_i)$  is the sectional object at depth  $z_i$ , while  $b(x, y, z_i)$  is the complex-valued FZP at depth  $z_i$ , and  $n(x, y)$  is the imaging noise [32]. Traditionally, the 2D scanning involves a high-density raster trajectory [Fig. 1(a)]. The consecutive scan lines of the rectangular path are directly registered as individual rows of “pixels” in the measured hologram. Therefore, the lateral scan range is equivalent to the field of view of the camera-based holographic imaging system.

### B. Compressed Sensing Framework

The inverse problem, called computational optical sectioning, relies on the depth dependency of the FZP to separate and reconstruct different sections of objects from a hologram. This problem is ill posed, with several times more unknowns ( $N$  pixels per section) than the constraints ( $N$  pixels in the hologram). Previously,

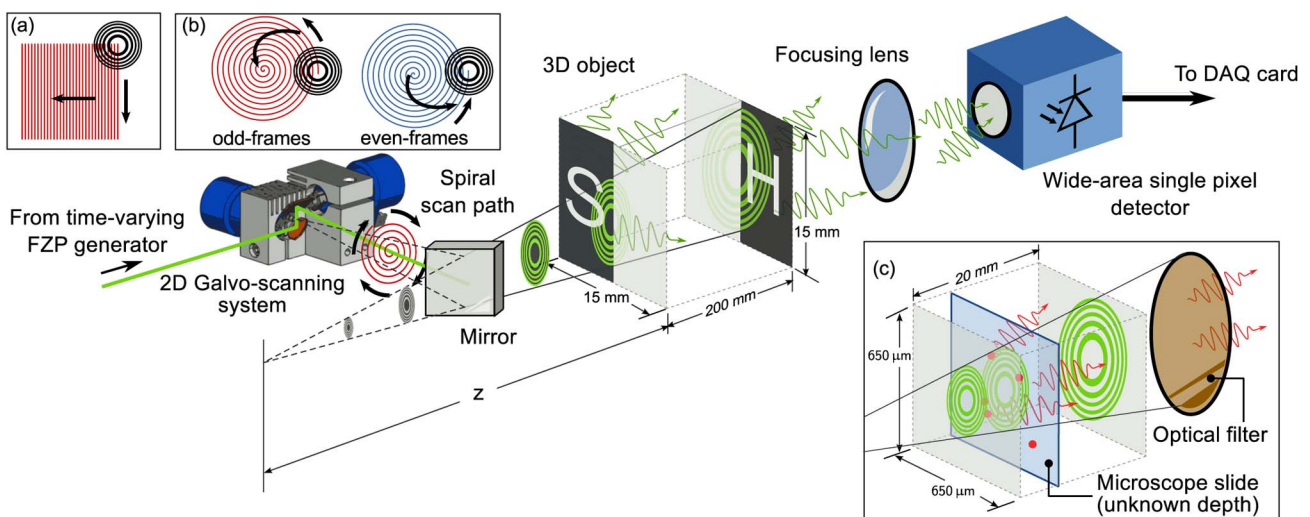


**Fig. 1.** Optical scanning holography with a spiral trajectory. The 3D object, consisting of two diffused binary masks, is placed at an unknown depth  $z$  from the galvo-scanning system. Inset: (a) High-density raster scanning trajectory, compared to (b) low-density spiral-scanning trajectory. Note that a mirror image of the spiral scan path is adopted at alternate frames to minimize path discontinuity. Owing to the large area of the FZP, the illumination is highly overlapping even with a low-density spiral trajectory. Therefore, holographic information is preserved with reduced data redundancy and acquisition time. (c) Alternative configuration for lensless holographic imaging of fluorescent beads.

we demonstrated that a 3D object with a finite number of thin sections can be restored by regularized optimization [32–35], i.e.,

$$\{\hat{O}_i\} = \arg \min_{\{O_i\}} \frac{1}{2} \left\| I - \sum_i (h_i * O_i) \right\|_F^2 + \alpha \sum_i \|W(O_i)\|_1, \quad (2)$$

where the coordinates  $(x, y)$  are omitted for brevity. Likewise,  $h_i$  and  $O_i$  denote the corresponding FZP and object sections at depth  $z_i$ . Here,  $\{\hat{O}_i\}$  is the set of reconstructed sections, while  $\alpha$  is the penalty factor of the regularization term;  $W(\cdot)$  is the sparsifying operator based on prior information about the object. The expression  $\|\cdot\|_F$  denotes the Frobenius norm.

With the same reconstruction framework, we further propose that the 3D object can still be restored with fewer than  $N$  pixels of the hologram, provided that three prerequisites of the CS model are fulfilled: *redundancy* in the scanning scheme, *sparsity* of the 3D object, and the *incoherence* between the FZP pattern and the scanning trajectory. The compressed sensing framework is expressed as

$$\{\hat{O}_i\} = \arg \min_{\{O_i\}} \frac{1}{2} \left\| I_S - B_S \left[ \sum_i (h_i * O_i) \right] \right\|_2^2 + \alpha \sum_i \|W(O_i)\|_1, \quad (3)$$

where the function  $B_S(\cdot)$  subsamples  $M$  out of  $N$  pixels from the hologram using the binary mask  $S$ .

*Redundancy* of scanning scheme dictates whether the 2D hologram can be directly subsampled without additional hardware. In most cases, the area of the FZP pattern  $h_i$  is comparable to that of the object  $O_i$ . Because of the large illumination area of the FZP pattern  $h_i$  compared to the scan line separation [Fig. 1(a) and 1(b)], the scanning process involves repeated measurements of every voxels in the 3D scenes. Since the amplitude and phase of each voxel of the 3D object are dispersed into multiple hologram pixels, the hologram pixels can be selectively discarded without severe loss of information.

The *sparsity* criterion, on the other hand, determines how much the 3D scene can be digitally compressed without losing reconstruction quality. Here, we assume that the 3D object consists of non-overlapping sections of thin objects and is dominated by empty space. With a right choice of the sparsifying operator  $W(\cdot)$ , the 3D object can be described mathematically with only  $K$  structural components, where  $K \ll N$ . Provided that the number of hologram pixels  $M$  in the mask  $S$  is marginally larger than  $K$ , the 3D objects can be restored with high accuracy [36,37].

### C. Choice of Scanning Trajectory

The *incoherence* requirement of CS requires the subsampling mask  $S$  to be significantly different from both the FZP pattern and the object so that reconstruction artifacts due to signal aliasing can be minimized [18]. According to the CS theory, the reconstruction of a 3D object with  $K$  structural components is guaranteed if

$$K \leq \frac{1}{2} \left[ 1 + \frac{1}{\mu(B_S, \{h_i\}, W)} \right], \quad (4)$$

where  $\mu(\cdot)$  is the measure of incoherence between the subsampled holographic scheme  $[B_S(\cdot)$  and  $\{h_i\}]$  and the sparsity constraint  $[W(\cdot)]$ , as defined in [38]. It can be shown that

$\sqrt{(N-M)/[M(N-1)]} \leq \mu(\cdot) \leq 1$  [17]. For optimal reconstruction performance, the subsampled hologram pixels are expected to be scattered in the scan area, which corresponds to a uniform random mask [36,39]. In practice, the mask must form a continuous path because the scanning hardware (e.g., the translation stage, galvanometer) forbids random access of spatial coordinates. The hardware constraint and the incoherence requirement can be bypassed with a low-density scanning trajectory. An example is a non-uniform rectangular path realized by skipping rows of the raster scan on the fly, which requires an adaptive software to select essential rows [21]. Here, we propose to subsample the hologram *non-adaptively* along a non-raster scanning trajectory shaped as an Archimedean spiral, i.e.,

$$S(x_j, y_j) = \begin{cases} 1 & \text{if } (x_j, y_j) = \left( \frac{R}{2\pi p} \theta_j \cos \theta_j, \frac{R}{2\pi p} \theta_j \sin \theta_j \right), \\ 0 & \text{otherwise,} \end{cases} \quad (5)$$

where  $\theta_j$  is the turn angle in polar coordinates,  $R$  is the radius of the circular field of view, and  $p$  is the number of revolutions within the field of view. As mentioned before, the smooth low-density trajectory helps reduce the acquisition time per frame and utilize the available inertial bandwidth of the bulky scan head. Compared to a non-uniform rectangular path, the spiral path is incoherent with most artificial and natural objects, and thus it favors a robust scanning scheme without additional hardware or adaptive software. It also uses all available imaging fields of view in the circular aperture, which is very common in optical systems. The mirror image of the same spiral trajectory can be adopted at alternate frames to return the FZP illumination pattern to the home position [Fig. 1(b)], which also acquires subsampled holographic measurements of the 3D object.

## 3. MATERIALS AND METHODS

### A. Performance Characterization

To evaluate the effectiveness of compressed sensing at different compression ratios and object complexities, we generate a 3D barcode phantom in a  $512 \times 512$  grid (15 mm  $\times$  15 mm) with alternating depths (870 and 1070 mm) and scan it with a spiral path to obtain a 2D hologram. The compression ratio is equal to  $M/N$ , where  $M$  is the number of pixels along the spiral path [Fig. 2(a)]. Since the 3D object consists of flat areas with sharp boundaries [Fig. 2(b)], the object is sparse in the gradient field. Therefore, a gradient operator is chosen as the sparsifying operator in Eq. (3), i.e.,

$$W(O) = \frac{\partial}{\partial x} O(x, y) + j \frac{\partial}{\partial y} O(x, y). \quad (6)$$

The sparsity level of the predefined barcode pattern is expressed as  $K/N$ , where  $K$  is approximated as the number of non-zero pixels in  $W(O)$ . The density of the barcode patterns scales linearly with the sparsity level, from 0.2 line pairs per millimeter (lp/mm) [leftmost figure, Fig. 2(b)], to 8.6 lp/mm [rightmost figure, Fig. 2(b)]. We use augmented Lagrangian multiplier with total-variation penalty [40] with default parameters to reconstruct the sample. The two reconstructed sections are then stitched to form an intermediate 2D image twice the imaging area before being compared to that of the ground truth. This treatment enables us to estimate the distortion in spatial features in

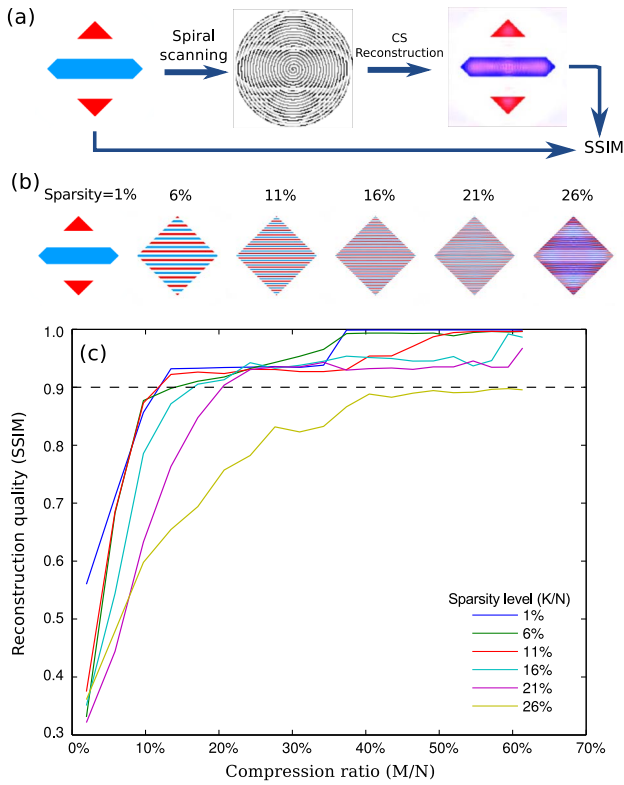


**Fig. 2.** Performance characterization of SuSHI with a spiral trajectory. (a) In the simulation, the 3D phantom consists of barcode patterns in two predefined depths. The phantom is then scanned by the time-varying FZP pattern with a spiral trajectory and then restored by the compressed sensing framework. The density of the spiral pattern determines the compression ratio ( $M/N$ ). The restored object is compared with the ground truth from the raster scan to obtain an SSIM. (b) Examples of high-quality reconstructed 3D barcode (SSIM  $\approx 0.9$ ) with increasing density. Red/blue colors represent the top/bottom layers, respectively. (c) SSIM score is plotted against compression ratio ( $M/N$ ). All phantoms below 20% sparsity level achieve accurate restoration (SSIM  $\geq 0.9$ ) at a 20% compression ratio.

corresponding sections and to address the crosstalk between sections. The structural similarity index (SSIM) score is chosen as the reconstruction quality metric because it is less susceptible to reconstruction artifacts than other methods, such as mean square error or peak signal-to-noise ratio [41], making it a better measure of image quality.

### B. Optical Sectioning of Binary Objects

We apply CS on actual OSH data acquired by Kim *et al.* [10]. As illustrated in Fig. 1, the 3D scene consists of two diffusive binary masks of dimensions 15 mm  $\times$  15 mm separated by 200 mm. A Mach–Zehnder interferometer is located at a distance 870 mm before the 3D object to generate a time-varying FZP pattern at wavelength 633 nm. The hologram was obtained with a full raster scan in a 500  $\times$  500 grid. The effective numerical aperture (NA) of the hologram is 0.025.

The rectangular hologram data is then subsampled by a spiral trajectory (top row, Fig. 3), which is defined by Eq. (5). The density of the spiral, determined by the number of revolutions  $p$ , is set manually from  $p = 10$  to  $p = 40$ . For each spiral trajectory, the two optical sections are reconstructed with Eq. (3). As there is no

ground truth for comparison, a 3D object reference is constructed from the case where  $p \rightarrow \infty$ , i.e., by recording all pixels inside the circular field of view. The reconstruction performance is quantified by comparing the compressed sensing result with the reference 3D object to obtain the SSIM score.

### C. Lensless Holographic Imaging of Fluorescent Beads

We reconfigured Kim *et al.*'s setup to demonstrate the capability of compressed sensing of the fluorescent object. The Mach–Zehnder interferometer is configured at an effective NA = 0.10 at a working distance of  $z = 40$  mm. An electro-optic phase modulator is placed at the reference beam path to generate a non-linear optical heterodyne signal (see Supplement 1).

We prepare a thin section of fluorescent beads (Life Technologies C-14837) by mounting a small drop of the reagent ( $\leq 10 \mu\text{M}$ ) onto the microscope slide, which is then flattened by the cover slip and left standing to dry for one night. The fluorescent sample is then placed at a fixed distance within  $z = 40 \pm 10$  mm from the 2D galvo-scanning system (Fig. 1). The sample is excited at 532 nm by a diode-pumped solid-state (DPSS) laser diode (Thorlabs DJ532-40) and filtered with a 600 nm long-pass filter (Thorlabs FEL0600).

The success of object reconstruction by Eq. (3) requires a precise value of the depth  $z$  of the sample, which can be obtained by computational autofocus (see Section 2 in Supplement 1) within the given range  $z = 40 \pm 10$  mm. Another requirement for success is the accurate representation of *sparsity*. Since the single thin section of the microbeads consists of tiny circular disks with a consistent diameter, we define the sparsifying operator as the cross-correlation of the sectional object with a matched filter  $\overline{h_\sigma(x, y)}$ , i.e.,

$$W(O) = \int_{-\infty}^{\infty} \int_{-\infty}^{\infty} \overline{h_\sigma(x, y)} O(x + u, y + v) dx dy, \quad (7)$$

where  $\overline{h_\sigma(x, y)} = \exp[-(x^2 + y^2)/(2\sigma^2)]$ , and  $2\sigma = 25 \mu\text{m}$  is the average diameter of the fluorescent beads. Again, we use the augmented Lagrangian multiplier method to reconstruct the thin section of microbeads at the estimated depth (see Section 3 in Supplement 1).

## 4. RESULTS AND DISCUSSION

The results of the performance characterization are shown in Fig. 2(c). Under noise-free condition, perfect reconstruction (SSIM = 1.00) is assured at a low sparsity level ( $K/N = 1\%$ ), with less than half of the total holographic pixels ( $M/N \leq 40\%$ ). At the 20% compression level, simple 3D objects ( $K/N \leq 20\%$ ) can all be reconstructed at high fidelity (SSIM  $\geq 0.90$ ). For dense 3D barcode patterns ( $K/N > 25\%$ ), more than 60% of the hologram pixels ( $M/N > 60\%$ ) must be acquired to guarantee reconstruction quality, which corresponds to more than 100 spiral revolutions and slightly less than  $2 \times$  acquisition speed-up. As mentioned before, the large discrepancy between the sparsity level and compression ratio implies that the complex pattern no longer fulfills the sparsity requirement of CS. In practice, the dense periodic patterns can still be aggressively subsampled and accurately restored by choosing a better sparsifying operator, such as 2D Fourier transform. The change of sparsifying transform does not require the change of the non-raster scan path or the re-sampling of the object itself, thus adding to the robustness of this subsampling technique.

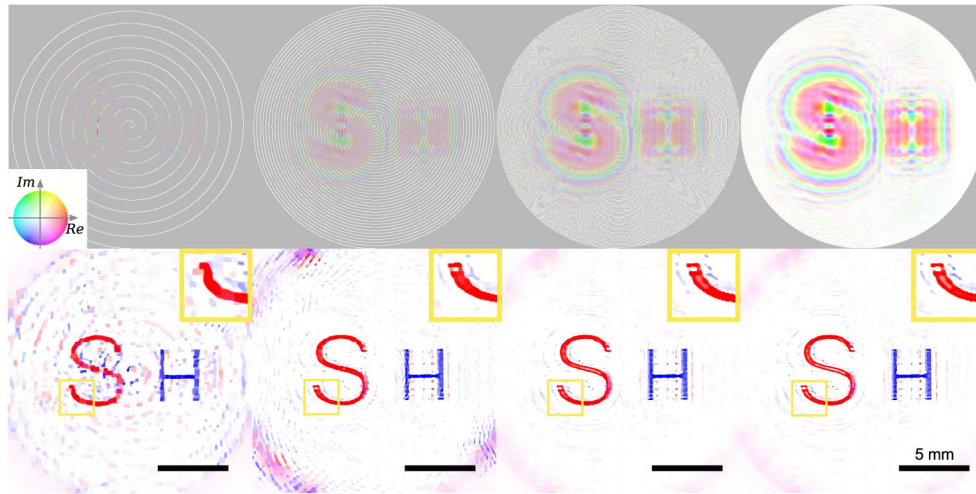


**Fig. 3.** Compressed spiral-scanning measurement and reconstruction of physical 3D object with spiral scanning. (Top row) Subsampled complex-valued hologram data along the spiral path. The magnitude and phase values are represented by the saturation and hue, respectively, as shown in the color wheel of the legend. Undefined hologram pixels are displayed as the gray color. The corresponding numbers of spiral revolutions  $p$ , compression ratio  $M/N$ , and the reconstruction performance score (SSIM) are shown in Table 1. (Bottom row) The reconstructed image shows the proximal layer in red ( $z_1 = 870$  mm) and the distal layer in blue ( $z_2 = 1070$  mm). Empty space is depicted as white. (Inset) The zoomed-in view of the restored 3D object. Note the high quality of letter “S” down at the 25% compression ratio.

**Table 1. Performance of SuSHI with Two-Section Binary Object**

Number of Spiral Revolutions $p$	10	40	90	250
Compression Ratio $M/N$	4%	25%	33%	100%
Scanning Speed-Up:				
Maximum Scan Rate	$35 \times$	$9 \times$	$4 \times$	$1 \times$
Fixed Pixel Dwell Time	$20 \times$	$5 \times$	$2.3 \times$	$1 \times$
Reconstruction Quality (SSIM)	0.68	0.86	0.99	1.00

Such significant acquisition speed-up is also observed from the hologram data captured from the experimental setup (Fig. 3). Again, the two-section object consists of non-overlapping binary patterns with sharp boundaries. The reconstructed sections, labeled “S” and “H”, are clearly visible (SSIM = 0.68) from a 10-revolution spiral. Since the two-section object in the  $500 \times 500$  grid (i.e.,  $N = 250,000$ ) is restored from hologram pixels along the spiral ( $M = 9,886$ ), we achieve a 4% compression ratio.

Assuming a fixed pixel dwell time, a conservative estimate of the effective frame rate would yield a  $20 \times$  speed-up, compared to raster scanning in the circular aperture (i.e.,  $\pi/4 \times N \approx 196,000$ ). However, a higher frame rate is achievable in this inertia-limited setup by reducing the pixel dwell time. For a typical galvo-scanning system, the mirrors can be driven with a sawtooth signal at around 175 Hz [42]. For a  $500 \times 500$  grid, at least 250 sweep cycles are required along the fast axis to complete one frame. Hence, the effective raster-scan frame rate is only around 0.7 Hz. On the other hand, a 10-revolution spiral-scanning trajectory can be driven by a smooth sinusoidal waveform at sweep rate up to 250 Hz [42], achieving an effective frame rate of 25 Hz. In other words, this spiral-scanning approach can reach a  $35 \times$  speed-up. In general, the acquisition time per 3D volume scales linearly with the number of spiral revolutions  $p$ .

At a 25% compression ratio (Table 1), the restored object is almost of the same quality as the image reconstructed from all pixels (SSIM = 0.86). Amid the presence of halo-like artifacts around the circular aperture (Fig. 3), the binary patterns still stand out from the background. Again, the reconstruction quality can be further improved digitally by modifying the sparsity constraints. In this case, since the two-section binary objects are surrounded by empty space, an extra regularization term  $\beta \sum_i \|O_i\|_1$ , where  $\beta > 0$  can be appended to Eq. (2) to suppress the background [43,44].

Unlike the binary objects in the previous example, fluorescent objects are known for their low quantum efficiency of emission, thus requiring much longer averaging times per pixel to combat detection noise. Prolonged laser scanning in a 3D volume also adds to the risk of photodamage and bleaching of the fluorescent dye. Hence, a low-density trajectory benefits the imaging of fluorescent samples by improving both the time resolution and reducing the total exposure time. Here, we employ the subsampling technique in a lensless holographic imaging setup to localize microbeads in a microscope slide at an unknown depth  $z$  [Fig. 1(c)]. At a constant pixel dwell time of 10 ms, a single hologram is captured along the 20-revolution spiral trajectory ( $M = 9,788$ ) at an effective frame rate of 0.01 Hz [Fig. 4(a)]. Compared to the raster scanning of the circular aperture in the  $256 \times 256$  grid ( $\pi/4 \times 256^2 \approx 51,000$ ), we achieve an 18% compression ratio, i.e., more than  $5 \times$  speed-up in the effective frame rate. The restored location of the fluorescent beads [Fig. 4(c)] shows strong agreement with those acquired by conventional wide-field fluorescence microscope [Figs. 4(f) and 4(g)]. We also demonstrate the capability of CS to localize fluorescent beads outside the circular field of view [red arrow, Fig. 4(c)]. This is a result of the extrapolation of partial FZP patterns in the spiral-scanning hologram. The 2D hologram can be estimated from the restored object by applying the forward model in Eq. (1), as shown in Fig. 4(b). The previously clipped FZP patterns can be restored by the CS algorithm. The phase value is also extracted from

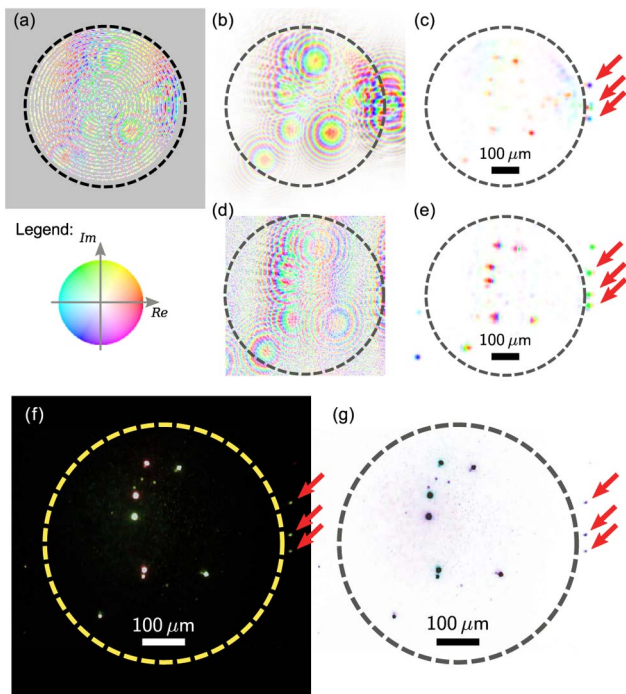


**Fig. 4.** Localization of fluorescent beads with lensless holography. (a) Subsampled hologram with spiral trajectory, (b) restored hologram, (c) restored locations of the fluorescent beads, (d) raster scan of the same area, and (e) the corresponding restored locations. The magnitude and phase values are represented by the saturation and hue, respectively, as shown in the color wheel of the legend. Undefined hologram samples are displayed as the gray color. (f) Image captured by CMOS camera under wide-field fluorescence microscope and (g) intensity-inverted version of the same image. The circles in dashed lines depict the imaging field of view of diameter 650  $\mu\text{m}$ .

individual microbead objects [Fig. 4(c)]. The phase value shown is likely an artifact of the coherent crosstalk of the laser. With the careful choice of an incoherent light source, the extracted phase information can reveal the relative depth within the optical section [45].

Without the holographic imaging technique, 3D localization of objects would require dynamic focusing of microscope slide with a wide-field fluorescence microscope [Fig. 4(e)]. While the hardware configuration is relatively simple, it is known to have performance trade-off among working distance, imaging field of view, and resolving power. In this microbead localization experiment, it requires an imaging system with a resolving power of 0.1 NA and a working distance of around 40 mm. These constraints are uncommon for conventional microscope objective lenses. The image shown in Fig. 4(b), for instance, is captured by a 10X objective lens (Newport M-10X) at a working distance of 5.5 mm. This is much shallower than that of the lensless holographic imaging setup (40 mm) at a similar resolving power. Owing to the flexibility of illumination pattern generation, the FZP can be engineered to match the required resolving power without violating the working distance constraint. On the other hand, the imaging field of view is currently limited by the circular aperture of the focusing lens in front of the photodetector (Fig. 1). However, this can be solved by reconfiguring the setup [10] to receive epi-fluorescence signals. An alternative solution is to replace the beam scanning mechanism with an object scanning

mechanism with a 2D motorized translation stage [45]. Since fluorescence imaging is not limited by hardware inertia, a low-density spiral trajectory is equally applicable to a motorized stage to enable acquisition speed-up.

In this experiment, the pixel dwell time (10 ms) is limited by the low-cost silicon photodetector (Thorlabs PDA100A). A long averaging time of the lock-in amplifier is selected to recover the optical beating signal buried in the dark current noise generated by the detector, of which the noise equivalent power is in the order of  $10^{-13} \text{ W}/\sqrt{\text{Hz}}$ . Nevertheless, the effective frame rate can be further improved by at least an order of magnitude [46] with a shot-noise-limited photodetector, such as the avalanche photodiode or the photomultiplier tube. This can enable single-shot 3D fluorescent object tracking at a near-video frame rate. For real-time fluorescent bead tracking, the imaging frame rate is ultimately limited by the CS reconstruction speed. In this paper, the CS reconstruction algorithm takes around 15 s to restore the image.

## 5. CONCLUSIONS

We present the SuSHI technique to improve the effective frame rate of 3D volume recording, which can lead to the live capture of dynamic events in a 3D volume. A 3D scene can be scanned with a low-density non-raster trajectory to alleviate the mechanical inertia constraint of optical beam scanning hardware. The reduced measurements also help improve the acquisition speed of fluorescence holographic imaging systems with limited photon budgets by reducing the total exposure time. With prior knowledge of the object, the 3D scene is reconstructed with high fidelity by the compressed sensing framework. The reconstruction performance is characterized with simulation at different degrees of object structural complexity. With a predefined spiral-scanning trajectory, we demonstrate this approach in practical applications of holographic imaging, namely, optical sectioning of binary objects on the millimeter scale and the localization of fluorescent beads on the micrometer scale. We show that the effective frame rate can be increased to around 35 times for inertia-limited measurements and to at least 5 times for noise-limited measurements. The non-raster scanning approach is equally applicable to a collection of illumination patterns other than time-varying FZP, serving specific applications ranging from extended depth-of-field imaging to image encryption.

We also note the potential of this approach for adaptive object scanning, in which the scanning trajectory can be modified in real time to optimize both the acquisition speed and measurement quality. For instance, the two-section binary object in Fig. 3 can be scanned with two interconnected high-density spiral shapes to improve the image quality without sacrificing speed. Another example is employing special spiral trajectories with variable densities to further suppress aliasing artifacts [18]. The technique could have potential to enhance the capability of holographic imaging for real-time monitoring of dynamic events, especially microparticle tracking.

**Funding.** National Natural Science Foundation of China (NSFC); Research Grants Council, University Grants Committee (RGC, UGC) (N\_HKU714/13).

**Acknowledgment.** We thank Mr. Anson Tang for preparing the microscope slide of fluorescent beads.

See Supplement 1 for supporting content.

## REFERENCES

- D. Gabor, "A new microscopic principle," *Nature* **161**, 777–778 (1948).
- J. W. Goodman, *Speckle Phenomena in Optics* (Roberts & Company, 2007).
- W. Xu, M. H. Jericho, I. A. Meinertzhagen, and H. J. Kreuzer, "Digital in-line holography for biological applications," *Proc. Natl. Acad. Sci. USA* **98**, 11301–11305 (2001).
- L. Repetto, E. Piano, and C. Pontiggia, "Lensless digital holographic microscope with light-emitting diode illumination," *Opt. Lett.* **29**, 1132–1134 (2004).
- W. Bishara, H. Zhu, and A. Ozcan, "Holographic opto-fluidic microscopy," *Opt. Express* **18**, 27499–27510 (2010).
- J. Rosen and G. Brooker, "Non-scanning motionless fluorescence three-dimensional holographic microscopy," *Nat. Photonics* **2**, 190–195 (2008).
- J. Hong and M. K. Kim, "Single-shot self-interference incoherent digital holography using off-axis configuration," *Opt. Lett.* **38**, 5196–5199 (2013).
- T.-C. Poon, "Optical scanning holography—a review of recent progress," *J. Opt. Soc. Korea* **13**, 406–415 (2009).
- T.-C. Poon and J.-P. Liu, *Introduction to Modern Digital Holography with MATLAB* (Cambridge University, 2014).
- Y. S. Kim, T. Kim, S. S. Woo, H. Kang, T.-C. Poon, and C. Zhou, "Speckle-free digital holographic recording of a diffusely reflecting object," *Opt. Express* **21**, 8183–8189 (2013).
- B. W. Schilling, T.-C. Poon, G. Indebetouw, B. Storrie, K. Shinoda, Y. Suzuki, and M. H. Wu, "Three-dimensional holographic fluorescence microscopy," *Opt. Lett.* **22**, 1506–1508 (1997).
- G. Indebetouw, P. Klysubun, T. Kim, and T.-C. Poon, "Imaging properties of scanning holographic microscopy," *J. Opt. Soc. Am. A* **17**, 380–390 (2000).
- D. J. Brady, K. Choi, D. L. Marks, R. Horisaki, and S. Lim, "Compressive holography," *Opt. Express* **17**, 13040–13049 (2009).
- Y. Rivenson, A. Stern, and B. Javidi, "Compressive Fresnel holography," *J. Display Technol.* **6**, 506–509 (2010).
- M. M. Marim, M. Atlan, E. Angelini, and J.-C. Olivo-Marín, "Compressed sensing with off-axis frequency-shifting holography," *Opt. Lett.* **35**, 871–873 (2010).
- C. Fernandez-Cull, D. A. Wikner, J. N. Mait, M. Mattheiss, and D. J. Brady, "Millimeter-wave compressive holography," *Appl. Opt.* **49**, E67–E82 (2010).
- Y. Rivenson, A. Stern, and B. Javidi, "Overview of compressive sensing techniques applied in holography [invited]," *Appl. Opt.* **52**, A423–A432 (2012).
- M. Lustig, D. Donoho, J. Santos, and J. Pauly, "Compressed sensing MRI," *IEEE Signal Process. Mag.* **25**(2), 72–82 (2008).
- J. Swoger, M. Martínez-Corral, J. Huisken, and E. H. K. Stelzer, "Optical scanning holography as a technique for high-resolution three-dimensional biological microscopy," *J. Opt. Soc. Am. A* **19**, 1910–1918 (2002).
- P. W. M. Tsang, J.-P. Liu, and T.-C. Poon, "Compressive optical scanning holography," *Optica* **2**, 476–483 (2015).
- P. W. M. Tsang, T.-C. Poon, and J.-P. Liu, "Adaptive optical scanning holography," *Sci. Rep.* **6**, 21636 (2016).
- G. Indebetouw, "Properties of a scanning holographic microscope: improved resolution, extended depth-of-focus, and/or optical sectioning," *J. Mod. Opt.* **49**, 1479–1500 (2002).
- G. Indebetouw, Y. Tada, J. Rosen, and G. Brooker, "Scanning holographic microscopy with resolution exceeding the Rayleigh limit of the objective by superposition of off-axis holograms," *Appl. Opt.* **46**, 993–1000 (2007).
- J. Ke, T.-C. Poon, and E. Y. Lam, "Depth resolution enhancement in optical scanning holography with a dual-wavelength laser source," *Appl. Opt.* **50**, H285–H296 (2011).
- H. Ou, T.-C. Poon, K. K. Y. Wong, and E. Y. Lam, "Depth resolution enhancement in double-detection optical scanning holography," *Appl. Opt.* **52**, 3079–3087 (2013).
- Z. Xin, K. Dobson, Y. Shinoda, and T.-C. Poon, "Sectional image reconstruction in optical scanning holography using a random-phase pupil," *Opt. Lett.* **35**, 2934–2936 (2010).
- H. Di, K. Zheng, X. Zhang, E. Y. Lam, T. Kim, Y. S. Kim, T.-C. Poon, and C. Zhou, "Multiple-image encryption by compressive holography," *Appl. Opt.* **51**, 1000–1009 (2012).
- Y. Pan, W. Jia, J. Yu, K. Dobson, C. Zhou, Y. Wang, and T.-C. Poon, "Edge extraction using a time-varying vortex beam in incoherent digital holography," *Opt. Lett.* **39**, 4176–4179 (2014).
- N. Chen, Z. Ren, H. Ou, and E. Y. Lam, "Resolution enhancement of optical scanning holography with a spiral modulated point spread function," *Photon. Res.* **4**, 1–6 (2015).
- G. Rabut and J. Ellenberg, "Automatic real-time three-dimensional cell tracking by fluorescence microscopy," *J. Microsc.* **216**, 131–137 (2004).
- M. R. Edwards, R. W. Carlsen, and M. Sitti, "Near and far-wall effects on the three-dimensional motion of bacteria-driven microbeads," *Appl. Phys. Lett.* **102**, 143701 (2013).
- X. Zhang, E. Y. Lam, T. Kim, Y. S. Kim, and T.-C. Poon, "Blind sectional image reconstruction for optical scanning holography," *Opt. Lett.* **34**, 3098–3100 (2009).
- X. Zhang, E. Y. Lam, and T.-C. Poon, "Reconstruction of sectional images in holography using inverse imaging," *Opt. Express* **16**, 17215–17226 (2008).
- X. Zhang and E. Y. Lam, "Edge-preserving sectional image reconstruction in optical scanning holography," *J. Opt. Soc. Am. A* **27**, 1630–1637 (2010).
- E. Y. Lam, X. Zhang, H. Vo, T.-C. Poon, and G. Indebetouw, "Three-dimensional microscopy and sectional image reconstruction using optical scanning holography," *Appl. Opt.* **48**, H113–H119 (2009).
- J. Romberg, "Compressive sensing by random convolution," *SIAM J. Imaging Sci.* **2**, 1098–1128 (2009).
- E. J. Candès and Y. Plan, "A probabilistic and ripples theory of compressed sensing," *IEEE Trans. Inf. Theory* **57**, 7235–7254 (2011).
- A. M. Bruckstein, D. L. Donoho, and M. Elad, "From sparse solutions of systems of equations to sparse modeling of signals and images," *SIAM Rev.* **51**, 34–81 (2009).
- E. J. Candès and T. Tao, "Near-optimal signal recovery from random projections: universal encoding strategies?" *IEEE Trans. Inf. Theory* **52**, 5406–5425 (2006).
- C. Li, W. Yin, H. Jiang, and Y. Zhang, "An efficient augmented Lagrangian method with applications to total variation minimization," *Comput. Optim. Appl.* **56**, 507–530 (2013).
- Z. Wang, A. Bovik, H. Sheikh, and E. Simoncelli, "Image quality assessment: from error visibility to structural similarity," *IEEE Trans. Image Process.* **13**, 600–612 (2004).
- "Scanning galvo systems user guide," Tech. rep., Thorlabs Inc. (2016). <https://www.thorlabs.com/thorcat/18700/GVS001-Manual.pdf>.
- R. Tibshirani, M. Saunders, S. Rosset, J. Zhu, and K. Knight, "Sparsity and smoothness via the fused lasso," *J. R. Stat. Soc. B* **67**, 91–108 (2005).
- J. Yang, Y. Zhang, and W. Yin, "A fast alternating direction method for TVL1-L2 signal reconstruction from partial Fourier data," *IEEE J. Sel. Top. Signal Process.* **4**, 288–297 (2010).
- G. Indebetouw and W. Zhong, "Scanning holographic microscopy of three-dimensional fluorescent specimens," *J. Opt. Soc. Am. A* **23**, 1699–1707 (2006).
- E. D. Diebold, B. W. Buckley, D. R. Gossett, and B. Jalali, "Digitally synthesized beat frequency multiplexing for sub-millisecond fluorescence microscopy," *Nat. Photonics* **7**, 806–810 (2013).